



An efficient cathode electrocatalyst for anion exchange membrane water electrolyzer

Shanmugam Ramakrishnan^{a,b,**}, Subramanian Vijayapradeep^a, Selva Chandrasekaran Selvaraj^c, Jian Huang^b, S.C. Karthikeyan^a, Rambabu Gutru^b, Natarajan Logeshwaran^a, Tsuyoshi Miyazaki^c, Mohamed Mamlouk^b, Dong Jin Yoo^{a,d,*}

^a Graduate School, Department of Energy Storage/Conversion Engineering (BK21 FOUR), Jeonbuk National University, Jeonju, Jeollabuk-do, 54896, Republic of Korea

^b School of Engineering, Newcastle University, NE1 7RU, United Kingdom

^c International Center for Materials Nanoarchitectonics (WPI-MANA), National Institute for Materials Science, Tsukuba, 305-0044, Japan

^d Department of Life Science, R&D Education Center for Whole Life Cycle R&D of Fuel Cell Systems, Hydrogen and Fuel Cell Research Center, Jeonbuk National University, Jeollabuk-do, 54896, Republic of Korea

ARTICLE INFO

Keywords:

Hierarchical MoS₂

Pt-C core-shell

Density functional theory

In-situ Raman analysis

Anion exchange membrane water electrolyzer

ABSTRACT

A high performance and durable electrocatalyst for the cathodic hydrogen evolution reaction (HER) in anion exchange membrane (AEM) water electrolyzers is crucial for the emerging hydrogen economy. Herein, we synthesized Pt-C core-shell nanoparticles (core: Pt nanoparticles, shell: N-containing carbon) were uniformly coated on hierarchical MoS₂/GNF using pyrolysis of *h*-MoS₂/GNF with a Pt-aniline complex. The synthesized Pt-C core-shell@*h*-MoS₂/GNF (with 11.3 % Pt loading) showed HER activity with a lower overpotential of 30 mV at 10 mA cm⁻² as compared to the benchmark catalyst 20 % Pt-C (41 mV at 10 mA cm⁻²) with improved durability over 94 h at 10 mA cm⁻². Furthermore, we investigated the structural stability and hydrogen adsorption energy for Pt₁₃ cluster, C₉₀ molecule, *h*-MoS₂ sheet, Pt₁₃-C₉₀ core-shell, and Pt₁₃-C₉₀ core-shell deposited *h*-MoS₂ sheets using density functional theory (DFT) simulations. We investigated the Pt-C core-shell@*h*-MoS₂/GNF catalyst active sites during HER performance using *in-situ* Raman analysis as well as DFT. We fabricated AEM water electrolyzers with cathode catalysts of Pt-C core-shell@*h*-MoS₂/GNF and evaluated device performance with 0.1 and 1.0 M KOH at 20 and 60 °C. Our work provides a new pathway to design core-shell electrocatalysts for use in AEM water electrolyzers to generate hydrogen.

1. Introduction

Global energy demand has raised concerns over the depletion of fossil fuels and their environmental impacts like climate change, ozone depletion and carbon footprints [1–5]. This drives the need to develop an alternate form of energy, which should be renewable, sustainable, affordable, and clean, as indicated by the sustainable development goals of the future. Among the present non-conventional sources energy sources like wind, thermal, and solar [6], hydrogen holds great potential as a future fuel due to its distinctive properties, including zero carbon emissions and an abundant supply of raw material in the form of water [7]. However, 80 % of hydrogen around world is still produced by

conventional steam reforming and coal gasification, which are not viable options because of their low pure hydrogen output and greenhouse gas emissions [8]. Electrochemical water splitting is an efficient method of clean hydrogen production that overcomes all the conventional drawbacks. Even though electrochemical water splitting has proved to be the safest method of producing high purity hydrogen, it suffers from energy efficiency problems and limited availability of affordable electrocatalysts [9,10].

Electrochemical water splitting involves hydrogen evolution reaction (HER) and oxygen evolution reaction (OER) as their core reactions in the cathode and anode, respectively. The benchmark electrocatalysts of these half reactions, including Pt (HER), IrO₂, and RuO₂ (OER),

* Corresponding author. Graduate School, Department of Energy Storage/Conversion Engineering (BK21 FOUR), Jeonbuk National University, Jeonju, Jeollabuk-do, 54896, Republic of Korea

** Corresponding author. Graduate School, Department of Energy Storage/Conversion Engineering (BK21 FOUR), Jeonbuk National University, Jeonju, Jeollabuk-do, 54896, Republic of Korea.

E-mail addresses: ramakrishnan.shanmugam@newcastle.ac.uk (S. Ramakrishnan), djyoo@jbnu.ac.kr (D.J. Yoo).

<https://doi.org/10.1016/j.carbon.2024.118816>

Received 17 August 2023; Received in revised form 18 December 2023; Accepted 12 January 2024

Available online 14 January 2024

0008-6223/© 2024 The Authors. Published by Elsevier Ltd. This is an open access article under the CC BY license (<http://creativecommons.org/licenses/by/4.0/>).

demonstrated efficient electrocatalytic activity. However, their poor durability and scarcity on earth hinder the commercialization of water electrolyzers for hydrogen production. Cathodic hydrogen evolution remains difficult when using non-noble catalysts. Two efficient strategies can be employed to overcome this situation: (i) developing electrocatalysts free of noble metals and (ii) minimizing the usage of noble metals by alloying with affordable metals or depositing on suitable support materials without compromising their hydrogen production efficiency [11]. Strategically, introducing noble metals into transition metal-based catalysts to alter the host structure can effectively improve the electrocatalytic activity towards HER [12–16]. Transition metal chalcogenide-based electrocatalysts are effectively used as cathodes in energy storage and conversion devices such as fuel cells [1], batteries [1, 12], water electrolyzers [1, 12, 17], and solar cells [18] due to their good electron conductivity, facile synthesis method and excellent electrochemical properties. Among the varying types of transition metal chalcogenides, molybdenum disulfide (MoS_2) is a potential alternative electrocatalyst for the HER reaction due to its high hydrogen adsorption–desorption energy, higher intrinsic activity, longer active edges, basal planes, a d-band electronic structure, low cost, and an easy scalable synthesis method [19]. Further, the MoS_2 architecture consists of the S–Mo–S layers with a van der Waals gap of 6.5 Å between the two layers, and MoS_2 with a 1T structural phase showed improved HER activity due to the increased adsorption capability of the exposed active sites and sulfur-edge sites with good electron/ion transportation [2, 20, 21]. However, MoS_2 -based electrocatalysts showed insufficient electrical conductivity and minimum active area due to rapid aggregation during hydrothermal treatment. In this regard, hierarchical growth of MoS_2 supported on conductive carbon-based graphite nanofibers (GNFs) is a promising way to improve conductivity, reduce agglomeration, and increase MoS_2 active sites along with surface area [22, 23]. However, the electrocatalytic performance of hierarchically structured MoS_2 on GNFs remains inferior compared to the benchmark catalyst, i.e., platinum-carbon (Pt–C) with 20 % loading. Consequently, it is crucial to optimize the decoration of platinum (Pt) nanoparticles with minimal loading on the hierarchically grown MoS_2 /GNF composite to achieve enhanced catalytic performance.

The long-term HER performance of platinum (Pt) nanoparticles is compromised by their inadequate stability, which is a consequence of the progressive reduction in electrochemical surface area (ECSA) stemming from Ostwald ripening and agglomeration processes. The development of core-shell nanostructures ensures the stability of metal nanoparticles, achieved through the incorporation metal nanoparticle in carbon layer. Moreover, the core-shell configuration ensures long-term electrochemical stability, and the carbon layer shell resists the dissolution or degradation of the core metal nanoparticles during electrochemical operations [1, 24, 25]. Therefore, encapsulating Pt nanoparticles with a graphitic carbon shell is a viable approach for mitigating the degradation induced by these phenomena, including Ostwald ripening, dissolution, and agglomeration [26]. Moreover, the integration of nitrogen atoms into the graphitic carbon structure (that is, surrounding the Pt nanoparticles with a nitrogen-containing graphitic carbon layer) enhanced the electrocatalytic activity for HER while simultaneously improving the stability of the nanoparticles [24, 26]. This strategy aims to enhance the electrocatalytic activity towards HER as following ways: (i) improving electrocatalytic activity through the addition of Pt nanoparticles (with low loading of Pt) on support materials (MoS_2 /GNF), (ii) the stability of Pt nanoparticles achieved on support materials, through the encapsulating Pt nanoparticle in carbon layer, and (iv) improving durability of electrocatalyst through the encapsulated Pt nanoparticles with the nitrogen-containing carbon layer [27–29].

Based on the above, we first synthesized hierarchical MoS_2 coated graphitic nanofibers ($h\text{-MoS}_2$ /GNF) using the hydrothermal method at 180 °C for 12 h. Then, Pt–C core-shell nanoparticles (Pt nanoparticles are core and N-containing carbon layer act as shell) were uniformly

coated on $h\text{-MoS}_2$ /GNF using pyrolysis of $h\text{-MoS}_2$ /GNF with a Pt-aniline complex at 500 °C for 1 h at N_2 medium. The inductively coupled plasma–optical emission spectrometry (ICP-OES) results confirmed that the Pt loading was 11.3 % in Pt–C core-shell@ $h\text{-MoS}_2$ /GNF electrocatalyst. The synthesized Pt–C core-shell@ $h\text{-MoS}_2$ /GNF electrocatalyst was characterized using various analytical techniques such as field emission scanning electron microscopy (FE-SEM), high resolution transmission electron microscopy (HR-TEM), X-ray diffraction, Raman analysis and X-ray photoelectron spectroscopy (XPS) analysis. The structural, morphological, and spectroscopic studies confirmed the encapsulation of Pt nanoparticles with an N-containing carbon layer supported on the $h\text{-MoS}_2$ /N-GNF. The Pt–C core-shell@ $h\text{-MoS}_2$ /GNF electrocatalyst showed HER activity with a low overpotential of 30 mV at a current density of 10 mA cm^{-2} as compared to the commercial catalyst of 20 % Pt–C (41 mV at 10 mA cm^{-2}). Notably, 11.3 % Pt loaded Pt–C core-shell@ $h\text{-MoS}_2$ /GNF electrocatalyst showed to 26.8 % reduction in HER overpotential when compared to the 20 % Pt–C commercial catalyst. Furthermore, we investigated the structural stability and hydrogen adsorption energy for Pt_{13} , C_{90} , MoS_2 sheets, $\text{Pt}_{13}/\text{C}_{90}$ (core/shell), and $\text{Pt}_{13}/\text{C}_{90}$ deposited MoS_2 sheets using DFT. We also investigated the Pt–C core-shell@ $h\text{-MoS}_2$ /GNF catalyst active sites during HER performance using *in-situ* Raman analysis. We fabricated an AEM water electrolyzer using Pt–C core-shell@ $h\text{-MoS}_2$ /GNF as the cathode catalyst and evaluated the device performance in 0.1 and 1.0 M KOH at 20 and 60 °C. From the collective evaluations and results, we believe that this work provides a promising pathway for designing a core-shell based electrocatalysts towards AEM water electrolyzers for hydrogen production.

2. Experimental section

2.1. Materials

Sodium molybdate dihydrate ($\text{Na}_2\text{MoO}_4 \cdot 2\text{H}_2\text{O}$, ≥ 99.5 %), thioacetamide ($\text{C}_2\text{H}_5\text{NS}$), graphite nanofiber (GNF) with 95 % trace metals basis (sizes 10–40 μm), potassium tetrachloroplatinate (II) (K_2PtCl_4 , 99.5 %), commercial Pt–C (20 wt%), ethanol ($\text{C}_2\text{H}_5\text{OH}$), hydrochloric acid (HCl, 35 %), tetrahydrofuran, isopropyl alcohol solution and a 5 wt % Nafion solution were ordered from Sigma-Aldrich. A styrene-ethylene-butylene-styrene (SEBS) ionomer, low-density polyethylene (LDPE) - vinylbenzyl chloride (VBC) - trimethylamine (TMA)-based radiation grafted AEM was used [30]. Titanium fiber felt used as the gas diffusion layer (GDL) and purchased from Bekaert Toko Metal Fibre Co., Ltd (78 % porosity and 0.3 mm). A carbon paper (GDL) without a microporous layer (MPL) (non-wet proof, Freudenberg) and IrO_2 and NiCo_2O_4 were purchased from Alfa Aesar.

2.2. Synthesis of $h\text{-MoS}_2$ /GNF

Purchased GNFs were immersed in concentrated HNO_3 for 2 days to remove metal impurities and functionalize the GNFs. The $h\text{-MoS}_2$ /GNF was synthesized using a hydrothermal reaction. Briefly, 30 mg of functionalized GNF was dispersed in 30 mL of deionized water (DI), and then 2 mmol of the sodium molybdate dihydrate and 8 mmol of the thioacetamide were separately dissolved in 40 mL DI water. Both solutions were mixed, and then 0.5 mmol of oxalic acid (a shape-promoting agent) was added [23] (stirring was conducted for 1 h). Finally, the solution was transferred to a 100 mL Teflon autoclave and was kept at 180 °C for 12 h. Finally, the $h\text{-MoS}_2$ /GNF product was washed several times with DI water before being dried in a vacuum oven at 50 °C for 24 h.

2.3. Prepared of Pt-aniline complex

The Pt-aniline complex was prepared following a previous report [24]. Briefly, 120 mg of chloroplatinic acid were dissolved in 30 mL of aniline (purified using the vacuum distillation method) followed by

stirring for 5 h to form the Pt-aniline complex. The unreacted aniline was removed by washing the Pt-aniline complex with 0.2 M HCl.

2.4. Synthesis of Pt-C core-shell@h-MoS₂/GNF

The prepared 20 mg of Pt-aniline complex and 30 mg of the h-MoS₂/GNF were dispersed in 40 mL of ethanol solvent followed by stirring for 1 h. The ethanol solvent was removed using a rotary evaporator. Finally, Pt-aniline coated h-MoS₂/GNF was pyrolysis at 500 °C in N₂ medium for 1 h to obtain Pt-C core-shells formed on the h-MoS₂/GNF, and this product is denoted as Pt-C core-shell@h-MoS₂/GNF.

2.5. Fabrication of membrane electrode assembly for AEM water electrolyzer

A membrane electrode assembly was fabricated using NiCo₂O₄ or IrO₂ as an anode and Pt-C core-shell@h-MoS₂/GNF as a cathode. The radiation grafted AEM of LDPE with VBC was synthesized according to a previous report [30,31]. The synthesized AEM of LDPE-VBC was functionalized with Benzyl trimethylammonium groups through immersing the membrane in TMA 45%wt solution in water for 24 h. Subsequently, Cl⁻ ions were exchanged with OH⁻ by immersing the AEM in 1.0 M KOH solution (KOH was replenished every 20 min, 3 times). The final AEM was washed several times with DI water to remove excess OH⁻ ions, a process confirmed using pH paper. Anode catalysts NiCo₂O₄ or IrO₂ were dispersed in tetrahydrofuran (THF) by ultra-sonication. To this, SEBS ionomer and polytetrafluoroethylene (PTFE) binder were added to make the ink. The ink was sprayed on a titanium fiber felt GDL with an optimized loading of 2 mg cm⁻². The cathode catalyst Pt-C core-shell@h-MoS₂/GNF was mixed with SEBS ionomer and PTFE binder using isopropanol as a solvent. The ink was sprayed on carbon GDL (non-wet proof, Freudenberg) with an optimized loading of 0.2 mg_{Pt}/cm². After coating on the respective GDLs, the anode and cathode catalysts were treated with TMA for 24 h. The obtained electrodes were washed with water several times and dried. All three components (anode, cathode, membrane) were treated with 1M KOH before forming the membrane electrode assembly (MEA). The MEA was placed in an electrolyzer cell fixture and was torqued to 2 Nm. The cell was fed with 1.0 M and 0.1 M KOH solutions with flow rate of 50 mL min⁻¹. Polarization curves (from linear sweep voltammetry) of AEM electrolyzer was recorded from 1.2 to 2.3 V with scan rate of 1 mV s⁻¹ and EIS data was recorded from 0.1 Hz to 10⁶ Hz with an amplitude of (V_{rms}) 10 mV and cell voltage of 1.5 V. The stability test of the AEM electrolyzer was investigated by using chronoamperometry with 1.85 V for 15 h. All the electrochemical tests were performed on a Gamry interface 5000E potentiostat.

2.6. Computational methodology

DFT based first-principles calculations using CONQUEST code [32–34] were performed to study the structural stability and hydrogen adsorption energy of Pt₁₃, C₉₀, MoS₂ sheet, Pt₁₃-C₉₀ core-shell, and Pt₁₃-C₉₀ core-shell@h-MoS₂ sheet. PBE [35] functionals were used for exchange and correlation terms in DFT energy. In the case of Pt₁₃-C₉₀ core-shell@h-MoS₂, DFT-D2 corrections for van der Waals interactions were applied [36]. The double zeta plus polarization function (DZP) basis sets [37] were used with a 120 Ha cut-off energy for the charge density grid. The accuracy of DZP when compared to triple zeta plus triple polarization functions (TZTP) basis sets is shown in Fig. S8c. A 1 × 1 × 1 k-mesh was used for all the structures except isolated MoS₂ sheet where a 12 × 12 × 1 k-mesh with a Monkhorst-Pack scheme was provided. The free energy of the hydrogen evolution reaction (ΔG_{H*}) was calculated using the following equation:

$$\Delta G_{H^*} = \Delta E_H + \Delta E_{ZPE} - T\Delta S_H \quad (1)$$

where ΔE_H, ΔE_{ZPE} = E_{ZPE}^H - ½E_{ZPE}^{H₂}, and ΔS_H = S_H^o - ½S_{H₂}^o are hydrogen adsorption energy from the DFT calculations, the change in zero point energy (ZPE) and entropy between the adsorbed state of hydrogen atom and the gas phase hydrogen molecule at 298 K, respectively [38]. Values of ΔE_{ZPE} - TΔS_H were chosen from previous studies as 0.24, 0.38, 0.38, and 0.29 eV for Pt, C, N, and S, respectively [38–40]. The hydrogen adsorption energy (ΔE_H) was calculated using the following equation.

$$\Delta E_H = E_{structure+H} - E_{structure} + \frac{1}{2}E_{H_2} \quad (2)$$

where E_{structure+H}, E_{structure}, and E_{H₂} are the calculated ground-state energies of optimized structures (such as Pt₁₃, C₉₀, h-MoS₂ sheet, Pt₁₃-C₉₀ core-shell and Pt₁₃-C₉₀ core-shell@h-MoS₂ sheet) with adsorbed hydrogen atoms, without hydrogen atoms and the ground-state energy of the H₂ molecule, respectively.

Before performing H adsorption studies, *ab-initio* molecular dynamics (AIMD) studies were further conducted at 600 K for C₉₀, N doped C₉₀, Pt₁₃-C₉₀ core-shell, and Pt₁₃-C₉₀ core-shell@h-MoS₂ sheet to examine their structural stabilities using CONQUEST [41]. Using the Nose-Hoover chain thermostats, canonical ensemble (NVT) simulations were carried out to study the time and temperature dependent energy profile [42]. The AIMD simulations were allowed up to 2ps with a time interval of 0.5 fs.

3. Results and discussion

3.1. Morphological and structural investigations of Pt-C core-shell@h-MoS₂/GNF nanohybrid

Fig. 1a–d presents a schematic diagram illustrating the synthesis of the Pt-C core-shell@h-MoS₂/GNF using the hydrothermal method at 180 °C for 24 h and pyrolysis method. In the first step, functionalized GNF with -COOH and -OH groups, which can enhance the binding strength and stability with Mo precursors. During the hydrothermal reaction, thioacetamide undergoes decomposition, releasing H₂S gas, which can react with the metal oxide to form h-MoS₂ on GNF [1]. In second step, pyrolysis of Pt-aniline complex on h-MoS₂/GNF at 500 °C for 1 h at N₂ medium result formation of Pt nanoparticles. These nanoparticles are encapsulated with an N-containing carbon layer on surface of the h-MoS₂/GNF. These N-containing carbon layers formed from aniline during the pyrolysis of Pt-aniline complex [24].

Fig. S1a shows the functionalized GNF a few micrometers in length and a few nanometers in thickness. After the hydrothermal reaction, MoS₂ was hierarchically grown on the GNFs and fully covered the surface as shown in Fig. S1b(i,ii). Furthermore, TEM images of h-MoS₂/GNF revealed that the GNF is covered with h-MoS₂ layers as shown Fig. S1c(i-iii), creating more active area for the electrocatalytic reaction. The schematic diagram of the interlayer distance and interlayer distance of MoS₂ was 0.63 nm, which belongs to the (002) plane of 2D layered MoS₂ as shown in Fig. S1d–e. These data agree with the X-ray diffraction pattern of MoS₂. Fig.S1f shows the SAED pattern of the MoS₂, confirming its semi-crystalline nature. The high-angle annular dark-field scanning TEM (HAADF-STEM) image of the h-MoS₂/GNF confirmed the presence of the carbon, molybdenum, and sulfur as shown Fig.S1g(i-ii). After pyrolysis of h-MoS₂/GNF with a Pt-aniline complex, FE-SEM images of the Pt-C core-shell@h-MoS₂/GNF showed that the hierarchical structure of MoS₂ slightly changed with the Pt-C core-shell and energy dispersive X-Ray spectroscopy (EDX) spectra with FE-SEM-EDAX elemental color mapping confirming the presence of Pt, Mo, S, N and C in the electrocatalyst as shown in Fig. 2a–d. The intrinsic structural morphology of the Pt-C core-shell@h-MoS₂/GNF was investigated using TEM and HR-TEM analysis as shown in Fig. 2e and f. Fig. 2e and Fig.S2ai show the presence of the Pt-C core-shell nanoparticles uniformly coated on the h-MoS₂ layer with average Pt nanoparticle sizes of about 3.8 nm (see Fig. 2e(iii)). Fig. 2eii and Fig. S2a (ii-iii) shows that the Pt nanoparticles

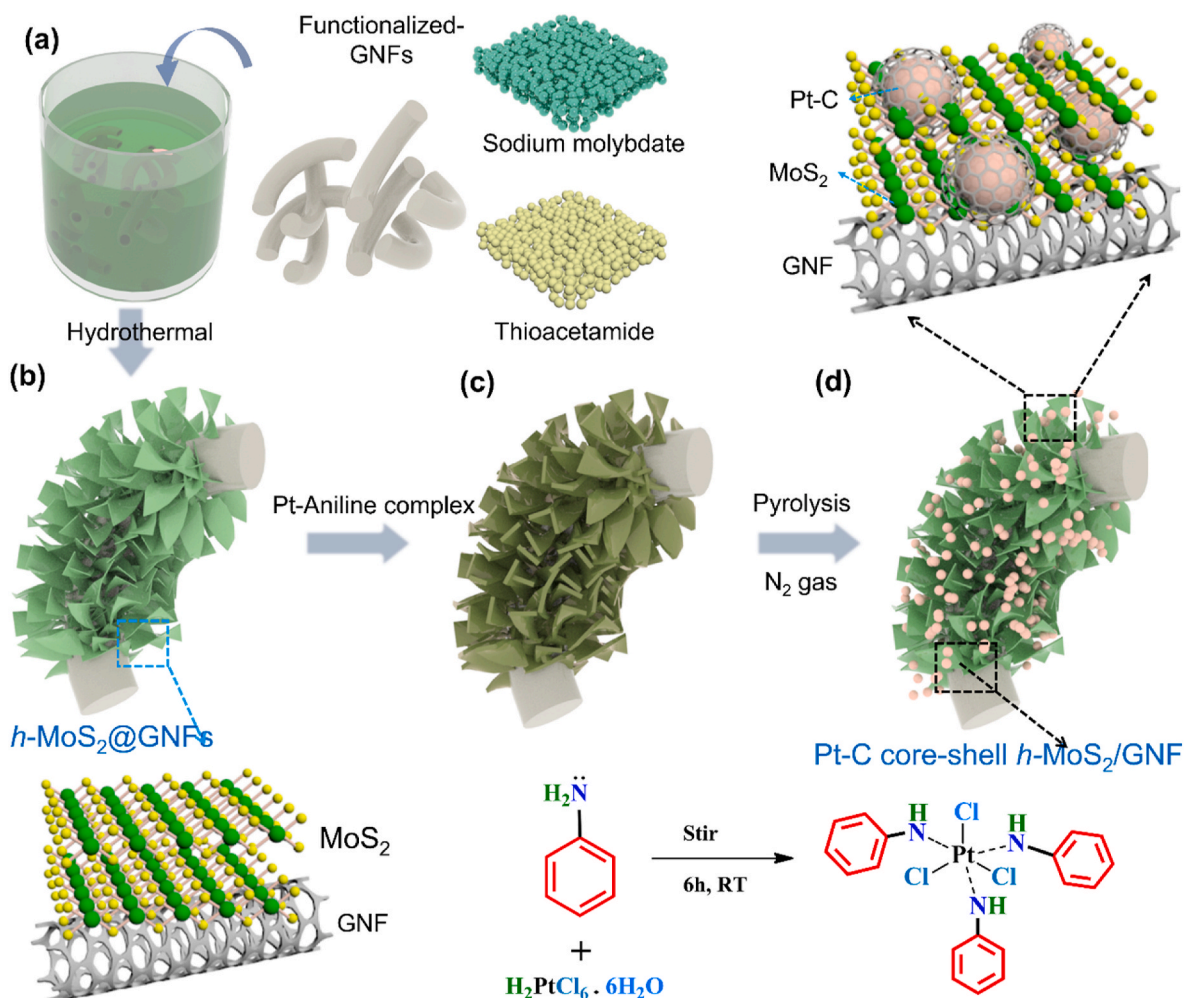


Fig. 1. Schematic diagram for synthesis of Pt-core-shell supported hierarchical MoS_2 coated GNF. (a) and (b) reactants and hydrothermal synthesis of $h\text{-MoS}_2/\text{GNF}$. (c) Coating of Pt-aniline complex on the $h\text{-MoS}_2/\text{GNF}$ and (d) Pt-C core-shell $h\text{-MoS}_2/\text{GNF}$ obtained after pyrolysis at 500°C under N_2 gas flow. (A colour version of this figure can be viewed online.)

were encapsulated with an N-containing carbon layer with a nanometer shell thickness. This would prevent Pt-nanoparticle dissolution, Oswald ripening and aggregation during the electrocatalytic stability test [24, 43]. The inset image of Fig. 2e(ii) shows the SAED pattern of the Pt-C core-shell $h\text{-MoS}_2/\text{GNF}$, which confirmed the crystalline nature of the Pt nanoparticles coated on the $h\text{-MoS}_2/\text{GNF}$. HR-TEM images of the Pt nanoparticles showed a lattice distance about 0.22 nm, which belongs to the Pt (111) phase, as shown in Fig. 2f(i,ii), and it agrees well with the XRD pattern [12,44]. The HAADF-STEM elemental color mapping of Pt-C core-shell $h\text{-MoS}_2/\text{GNF}$ shows the presence of the Pt, Mo, S, N and C elements in the prepared electrocatalyst as show in Fig.S12f.

We have utilized X-ray diffraction (XRD) analysis to investigate the crystalline nature of prepared electrocatalysts of Pt-C core-shell $h\text{-MoS}_2/\text{GNF}$, and the results are represented in Fig. S3a. The XRD pattern of the $h\text{-MoS}_2/\text{GNF}$ shows strong diffraction peaks at $\sim 14.0^\circ$, 33.8° , 39.7° , and 59.9° , which belong to (002), (100), (103), and (110) planes, respectively, of the crystalline MoS_2 (JCPDS No. 37-1492) [23]. Moreover, the characteristic peak of 14.0° that belongs to the stacked, layered morphology of the $h\text{-MoS}_2$ was also observed with strong graphitic characteristic peaks at 26.0° belonging to the (002) plane of the GNF [23,44]. After pyrolysis of the $h\text{-MoS}_2/\text{GNF}$ with the Pt-aniline complex at 500°C , the characteristic peaks of the MoS_2 were suppressed and Pt nanoparticle characteristic peaks appeared at 39.7° , 46.7° , 67.4° and 82.2° corresponding to the (111), (200), (220), and (311) planes, respectively, of crystalline Pt. These XRD analyses confirmed the formation of the

Pt-C core-shell on the $h\text{-MoS}_2/\text{GNF}$ during the pyrolysis process. Raman spectroscopy is a powerful tool to examine the crystal structure, defects, and electronic properties of the Pt-C core-shell $h\text{-MoS}_2/\text{GNF}$, $h\text{-MoS}_2/\text{GNF}$ and GNF. Fig. S3b shows the micro-Raman spectra of the prepared electrocatalyst of Pt-C core-shell $h\text{-MoS}_2/\text{GNF}$, $h\text{-MoS}_2/\text{GNF}$ and GNF. The functionalized GNF showed two peaks at 1341 and 1589 cm^{-1} , belonging to D (presence of defects or edges in the graphite lattice) and G (in-plane vibration of sp^2 -hybridized carbon atoms) bands, respectively. After growth of the $h\text{-MoS}_2$ on GNFs, the peak positions of the G and D bands appeared with positive shifts at 1353 and 1596 cm^{-1} , respectively [1]. After undergoing pyrolysis of the $h\text{-MoS}_2/\text{GNF}$ with a Pt-aniline complex, the D and G band peaks appeared at 1353 and 1595 cm^{-1} , respectively. Notably, the intensity ratio of the D and G (I_D/I_G) of Pt-C core-shell $h\text{-MoS}_2/\text{GNF}$ was 1.11, which was lower than that of GNF (1.37) and $h\text{-MoS}_2/\text{GNF}$ (1.33). Additionally, the full width at half maximum (FWHM) of D and G bands in Pt-C core-shell $h\text{-MoS}_2/\text{GNF}$ showed considerably increased as compared to $h\text{-MoS}_2$ on GNFs. This suggests a reduced degree of the graphitization compared to GNF due the formation of an N-containing carbon layer on the $h\text{-MoS}_2/\text{GNF}$ during pyrolysis of the Pt-aniline complex. This could correlate well with the observed decrease in the I_D/I_G ratio from 1.37 to 1.11 [45]. Moreover, we observed characteristic MoS_2 peaks of the E_{2g} and A_{1g} at 380 and 408 cm^{-1} , respectively in $h\text{-MoS}_2/\text{GNF}$. In contrast, Pt-C core-shell $h\text{-MoS}_2/\text{GNF}$ showed E_{2g} and A_{1g} peaks with slight negative shifts at 374 and 407 cm^{-1} . The intensity of E_{2g} and A_{1g} peaks

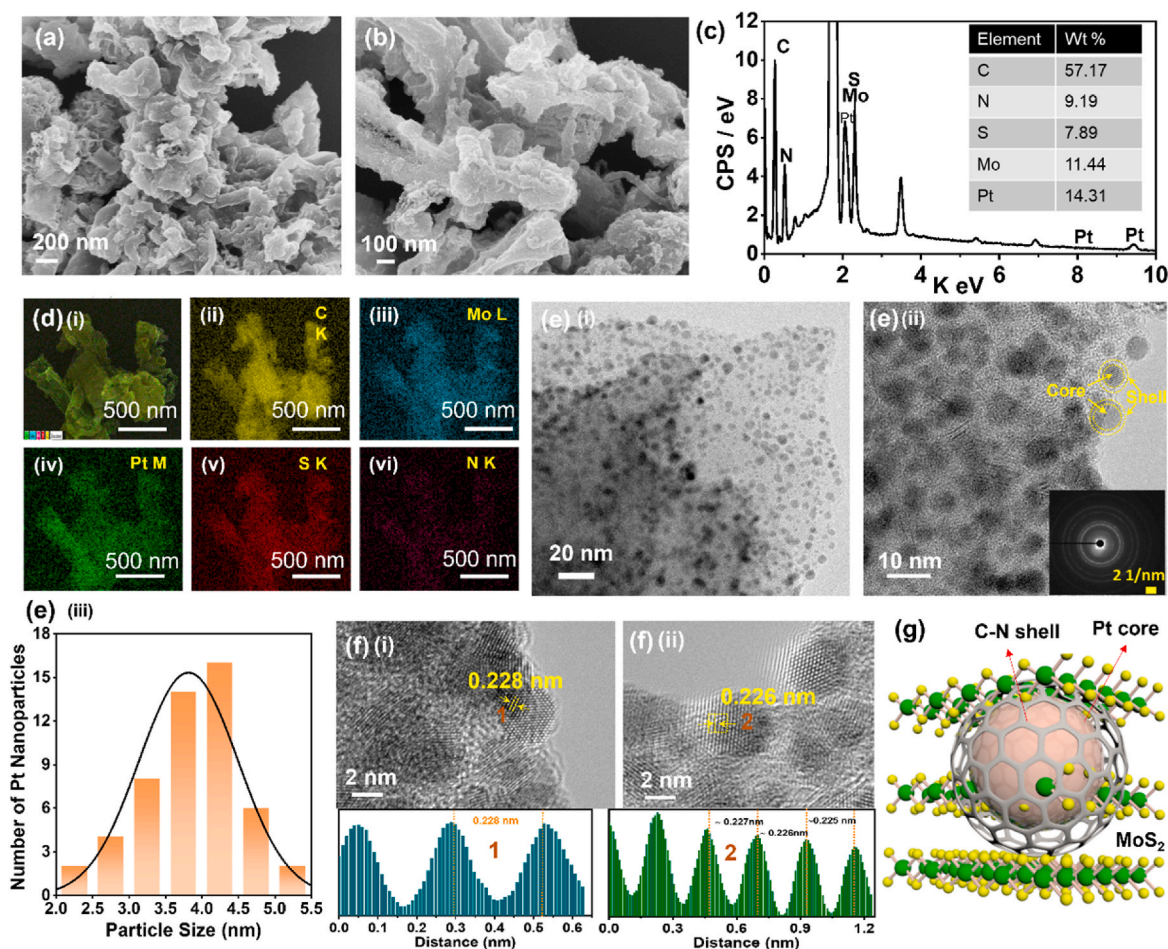


Fig. 2. (a–b) FE-SEM images and (c–d) EDX spectra with elemental color mapping of Pt–C core-shell/*h*-MoS₂/GNF. (e–f) HR-TEM images of Pt–C core-shell/*h*-MoS₂/GNF, inert image of (e) (ii) is the selected area diffraction (SAED) pattern of Pt–C core-shell/*h*-MoS₂/GNF and (e) (iii) histogram curves of sizes of Pt nanoparticles, which confirmed the average Pt nanoparticle size was about 3.8 nm and (f) (i–ii) lattice spacing distance of Pt(111) planes. (g) Schematic diagram of Pt–C core-shell/*h*-MoS₂. (A colour version of this figure can be viewed online.)

increased as compared *h*-MoS₂/GNF, confirming an increase in the crystalline nature of the MoS₂. [46–49].

3.2. XPS analysis of Pt–C core-shell/*h*-MoS₂/GNF

The chemical states and composition of elements of the Pt–C core-shell/*h*-MoS₂/GNF were investigated using XPS analysis. Fig. 3a–f and Table S1 shows the interpreted results of Pt–C core-shell/*h*-MoS₂/GNF and *h*-MoS₂/GNF electrocatalysts. The survey spectra illustrated in Fig. 3a confirmed the presence of Pt 4f, Mo 3d, S 2p, C 1s, and N 1s in the Pt–C core-shell structure of *h*-MoS₂/GNF. Fig. 3b shows the deconvoluted Pt 4f spectra, which displays two major peaks at 71.5 eV and 74.8 eV belonging to Pt 4f_{7/2} and Pt 4f_{5/2}, respectively. Further, the peaks corresponding to Pt (0) appeared at 71.2 eV (Pt 4f_{7/2}) and 74.5 eV (Pt 4f_{5/2}), whereas the peaks at 72.2 eV and 75.5 eV of Pt 4f_{7/2} and Pt 4f_{5/2} corresponding to Pt (II) appeared due to the Pt oxidation in the Pt–C core-shell/*h*-MoS₂/GNF [12,13]. The deconvoluted N1s spectra in Fig. 3c proved the incorporation of N-atoms in the encapsulated carbon layer. Deconvoluted N1s showed peaks at 400.7, 400.0, and 398.8 eV corresponding to graphitic-N, pyrrolic-N, and pyridinic-N, respectively [24,50]. This confirmed the presence of N-containing carbon layers covered by Pt nanoparticles during the pyrolysis of *h*-MoS₂/GNF with a Pt-aniline complex at 500 °C [24]. Fig. 3d shows the Mo 3d spectra of Pt–C core-shell/*h*-MoS₂/GNF and *h*-MoS₂/GNF, which clearly depicts

changes in the host structure after the addition of Pt–C. Fig. 3d shows the Mo 3d peaks of the *h*-MoS₂/GNF at 232.1 and 228.9 eV, which correspond to the 3d_{3/2} and 3d_{5/2}, respectively, and a peak around 226.1 eV belonging to S 2s of MoS₂. After pyrolysis of the *h*-MoS₂/GNF, the peaks of 3d_{3/2} and 3d_{5/2} appeared with positive shifts at 232.5 and 229.2, respectively, and the S 2s peak (226.1 eV) intensities increased as compared to *h*-MoS₂/GNF [1,13,44]. The peak at 235.7 eV corresponded to Mo⁶⁺, indicating the presence of the M–O bond in the Pt–C core-shell/*h*-MoS₂/GNF. Fig. 3e shows the deconvoluted peaks of S 2p for Pt–C core-shell/*h*-MoS₂/GNF and *h*-MoS₂/GNF. The deconvoluted peaks at 161.7 eV and 162.9 eV correspond to S 2p_{3/2} and S 2p_{1/2}, respectively [51,52]. After the pyrolysis process, Pt–C core-shell formed on the surface of *h*-MoS₂/GNF, deconvoluted to S 2p_{3/2} and S 2p_{1/2} peaks are shifted positively appeared at 162.5 eV and 163.7 eV respectively as compared to *h*-MoS₂/GNF. Further, oxidized sulfur peaks (168.8 eV) intensity increased as compared to *h*-MoS₂/GNF. The Pt–C core-shell/*h*-MoS₂/GNF shows carbon C1s spectra and its deconvoluted peaks at 284.3, 284.9, and 285.8 eV which correspond to C=C, C–N, and C–O, respectively [25], as shown in Fig. 3f. XPS results confirmed the formation of Pt nanoparticles, and these nanoparticles were encapsulated within an N-containing carbon layer, establishing the Pt–C core-shell structure in the Pt–C core-shell/*h*-MoS₂/GNF electrocatalyst. Furthermore, we investigated the loading of the Pt and Mo in Pt–C core-shell/*h*-MoS₂/GNF using ICP-OES. The results revealed that

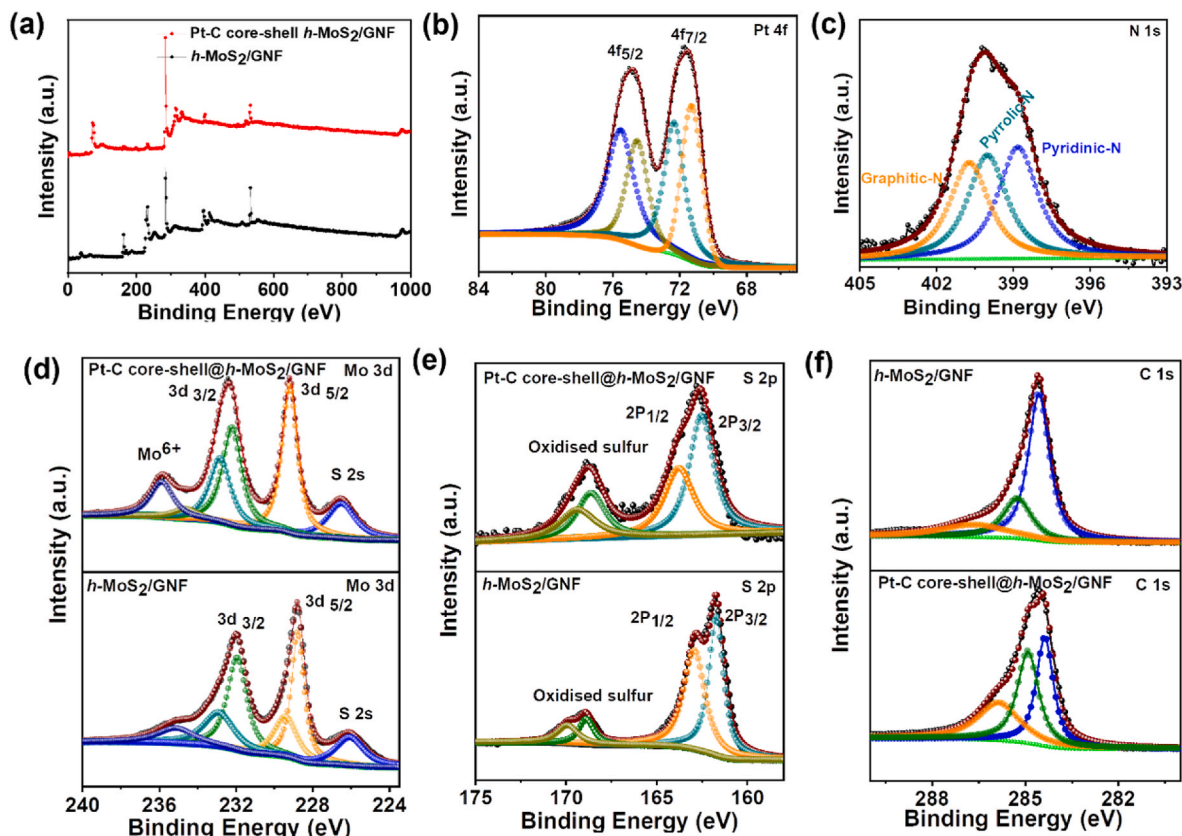


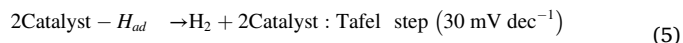
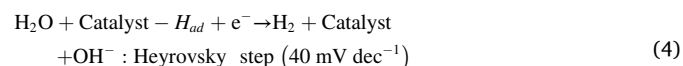
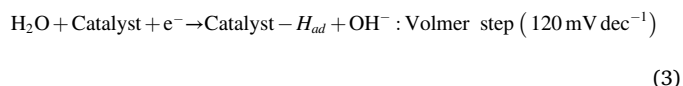
Fig. 3. XPS analysis of (a) survey spectra, (b) Pt 4f and (c) N 1s of Pt-C core-shell@*h*-MoS₂/GNF. High-resolution XPS spectra of (d) Mo 3d, (e) S 2p and (f) C 1s of *h*-MoS₂/GNF and Pt-C core-shell @*h*-MoS₂/GNF. (A colour version of this figure can be viewed online.)

loadings of Pt and Mo were 11.3 and 21.2 % respectively (See Table S2).

3.3. Electrochemical performance of Pt-C core-shell@*h*-MoS₂/GNF

A standard three electrode setup was utilized to evaluate the electrochemical performance of Pt-C core-shell@*h*-MoS₂/GNFs in a 1.0 M KOH alkaline electrolyte medium. Pt-C core-shell@*h*-MoS₂/GNF, *h*-MoS₂/GNF, and commercial 20 % Pt-C electrodes with similar loadings were fabricated and measured to compare the HER performances. All the recorded linear sweep voltammetry (LSV) curves were measured at the lowest scan rate of 1 mV s⁻¹ and were iR corrected as shown in Fig. 4a. Fig. 4a shows the measured LSV curves of all the prepared electrocatalysts at a current density of 10 mA cm⁻², in which Pt-C core-shell@*h*-MoS₂/GNF (with 11.3 % Pt loading) showed the low overpotential of 30 mV at current density of 10 mA cm⁻², which comparable overpotential with commercial 20 % Pt-C (41 mV) and lower than to *h*-MoS₂/GNF (180 mV), GNF (450 mV) at same current density. Thus, the as-prepared Pt-C core-shell@*h*-MoS₂/GNF electrocatalyst required an overpotential that was 11 mV (i.e., 26.8 %) lower than the commercial state of the art 20 % Pt-C and also compared HER performance with recently reported electrocatalyst (See Table S3). Fig. 4b shows a graphical illustration of the overpotential required for each of the prepared electrocatalysts at a current density of 10 mA cm⁻². Furthermore, Tafel slope values of the prepared electrocatalysts were calculated to evaluate the reaction kinetics and reaction mechanism. Based on the Tafel equation, the Tafel slope was extrapolated from the log (j) vs. overpotential [53] graph as represented in Fig. 4c. Fig. 4c illustrates that the Pt-C core-shell@*h*-MoS₂/GNF and commercial 20 % Pt-C electrocatalysts, both exhibit the low Tafel slope value of 32 and 38 mV dec⁻¹ respectively. In contrast, *h*-MoS₂ and GNF display significantly Tafel slopes values of 99 mV dec⁻¹ and 138 mV dec⁻¹, respectively. These finding suggest that the electrocatalytic HER activities of Pt-C

core-shell@*h*-MoS₂/GNF (with 11.3 % Pt loading) and commercial 20 % Pt-C electrocatalysts are similar, as evidenced by their comparable Tafel slope. Both electrocatalysts adhere to the Tafel-Volmer reaction pathway (as shown in Equations (3)–(5)), indicating efficient HER.



The electrochemical double layer capacitance (C_{dl}) was estimated by measuring CV curves at different scan rates in the non-faradaic region to calculate the electrochemically active surface area of the as prepared electrocatalysts. Fig. 4d and Fig. S4a–e shows the calculated C_{dl} values of Pt-C core-shell@*h*-MoS₂/GNF, 20 % Pt-C, *h*-MoS₂/GNF, and GNFs of 28.8, 24.1, 20.3, and 12.0 mF cm⁻², respectively. The optimized Pt-C core-shell@*h*-MoS₂/GNF retained a higher ECSA value of 720 cm² as compared to *h*-MoS₂/GNF (508 cm²), and GNF (300 cm²) and 20 % Pt-C (603 cm²) (see Fig. 4Se) [54]. To understand the electrode kinetics during the HER process, we explored the electrochemical impedance spectroscopy (EIS) of Pt-C core-shell@*h*-MoS₂/GNF, commercial 20 % Pt-C, *h*-MoS₂, and GNF, as depicted in Fig. S4f. Fig. S4f presents a Nyquist plot highlighting the interfacial charge transfer resistance (R_{CT}) of the electrodes. The charge transfer resistance (R_{CT}) of the *h*-MoS₂ and GNF were approximately 8.9 and 39.5 Ω respectively. Intriguingly, upon incorporating Pt nanoparticles, the R_{CT} of Pt-C core-shell@*h*-MoS₂/GNF reduced to approximately 2.0 Ω. This decrease indicates enhanced HER

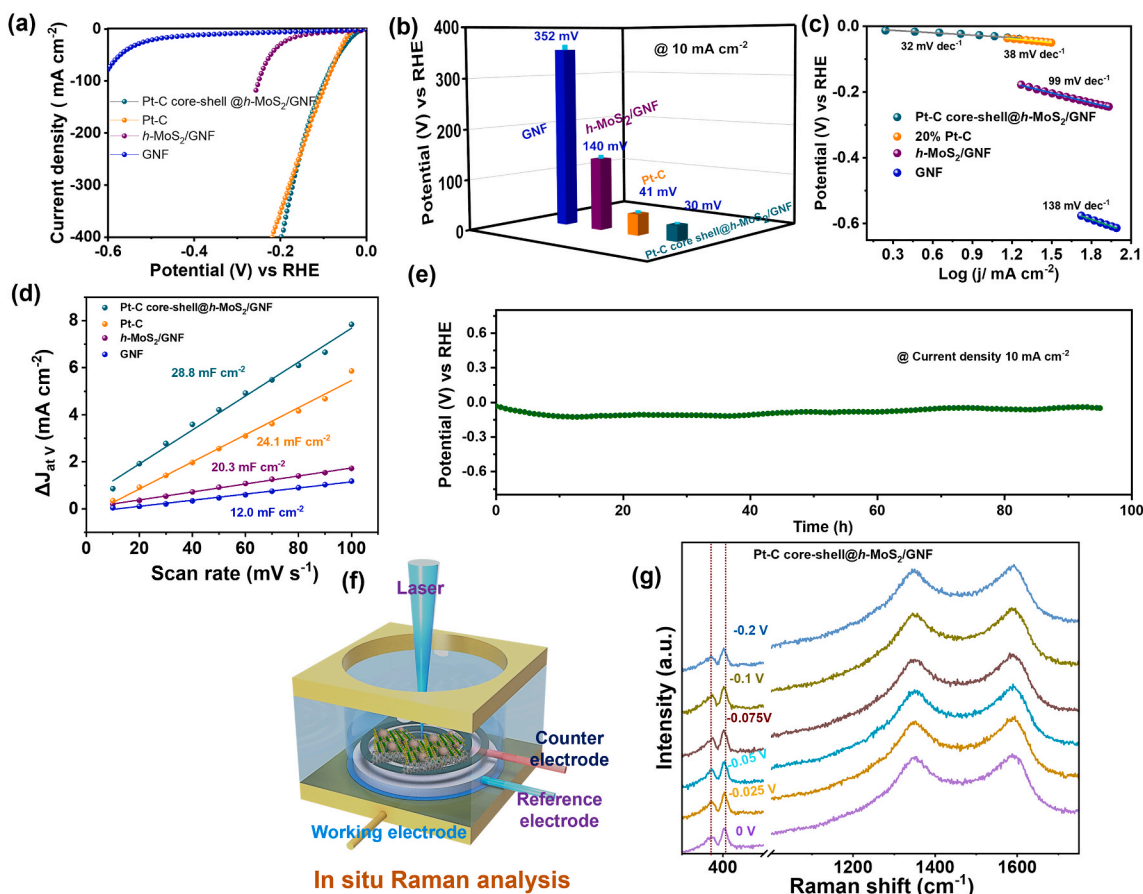


Fig. 4. HER performance: (a) HER LSV (iR corrected) curves of Pt-C core-shell *h*-MoS₂/GNF, *h*-MoS₂/GNF, GNF and 20 % Pt-C are measured with at 1 mV s⁻¹ in 1.0 M KOH electrolyte. (b) Bar chart for comparison of HER overpotential with Pt-C core-shell *h*-MoS₂/GNF, *h*-MoS₂/GNF, GNF and 20 % Pt-C at 10 mA cm⁻². (c) Tafel slope of Pt-core-shell on *h*-MoS₂/GNF, *h*-MoS₂/GNF, GNF, and 20 % Pt-C in 1.0 M KOH electrolyte and (d) double-layer capacitance measurements from plots of scan rate vs. Δj of Pt-core-shell on *h*-MoS₂/GNF, *h*-MoS₂/GNF, GNF and 20 % Pt-C in 1.0 M KOH electrolyte. (e) Chronopotentiometry curve of Pt-C core-shell *h*-MoS₂/GNF at a current density of 10 mA cm⁻² for 95 h. (f) Schematic diagram *in situ* Raman analysis, and (g) *in situ* Raman spectra of Pt-core-shell *h*-MoS₂/GNF with 1.0 M alkaline medium. (A colour version of this figure can be viewed online.)

activity and reduced R_{CT} after the integration of Pt nanoparticles into the *h*-MoS₂/GNF framework. Furthermore, we compared this R_{CT} value with that of commercial 20 % Pt-C, which exhibited an R_{CT} of approximately 2.5 Ω . Remarkably, the Pt-C core-shell/*h*-MoS₂/GNF electrode demonstrated a comparable R_{CT} value to that of the commercial 20 % Pt-C [12,13]. The electrochemical results revealed that the Pt-C core-shell/*h*-MoS₂/GNF with 11.3 % loading of Pt achieved the HER performance comparable to that of commercial 20 % Pt-C. Notably, Pt-C core-shell/*h*-MoS₂/GNF exhibited 26.8 % lower HER overpotential (30 mV at 10 mA cm⁻²) as compared to the 20 % Pt-C (41 mV at 10 mA cm⁻²). These improvement of Pt-C core-shell/*h*-MoS₂/GNF due to the highly dispersed and stable Pt nanoparticles, which might be attributed to the supportive framework of *h*-MoS₂/GNF, the carbon shell with N-containing, or a combination of both [13,24,51,55].

In addition to the electrochemical performance, the structural integrity, robustness, and durability of the optimized Pt-C core-shell/*h*-MoS₂/GNF electrocatalyst was investigated using cyclic stability and chronopotentiometry measurements. Fig. S4g shows the LSV curves taken before and after 1000 continuous cycles of cyclic voltammetry, illustrating the structural integrity of the electrocatalyst with minimal variation of only 14 mV. The chronopotentiometry measurements of optimized Pt-C core-shell/*h*-MoS₂/GNF from Fig. 4e indicate that there were no significant potential changes over 90 h for a constant current density of 10 mA cm⁻². Also, the LSV curves before and after 90 h chronopotentiometry measurements showed insignificant changes in the potential, again signifying the robustness of the optimized electrocatalyst.

Fig. S5a–b shows TEM images of the Pt-C core-shell/*h*-MoS₂/GNF after durability. The hierarchical structure of the MoS₂ on GNF changed (see Fig. S5a) over time during hydrogen evolution due to accumulation of bubbles and continuous release of the H₂ gas [56]. The Pt nanoparticles rarely agglomerated on *h*-MoS₂/GNF due to the N-containing carbon layer protecting the Pt nanoparticles against Oswald ripening and agglomeration during the long-term durability test. The HR-TEM image of Fig. S5b and c shows that Pt nanoparticle average sizes were 3.5–4.0 nm, and the d-space value of 0.22 nm belonged to the Pt (111) phase. The HAADF-STEM color mapping images of the Pt-C core-shell/*h*-MoS₂/GNF catalyst indicate the presence of Pt, Mo, S, N and C after the durability test as shown in Fig. S5d and e.

Fig. S6(a–f) presents the XPS spectra of Pt-C core-shell/*h*-MoS₂/GNF, including a survey spectrum (a) and high-resolution spectra for Pt 4f, Mo 3d, S 2p, N 1s, and C 1s (b–f). Specifically, Fig. S6b highlights the Pt 4f high-resolution XPS spectra, showing peaks at 71.4 and 74.7 eV, corresponding to the 4f_{7/2} and 4f_{5/2} states, respectively. XPS analysis (See Tables S1 and S4 in supporting information) indicates a reduction in the atomic percentage of Pt from 3.91 to 2.92, alongside a decrease in the Pt/C atomic ratio from 5.35 to 3.87 % (a 27.4 % loss) following the stability test. Conversely, after the durability test, the atomic percentage of Pt decreased only to 25.3 %, confirming that approximately 74.7 % of Pt remained stable. This stability is attributed to the encapsulation of Pt nanoparticles within an N-containing carbon layer, which protects against Pt nanoparticle dissolution during the HER stability test [24]. In contrast, the XPS spectra of Mo 3d (Fig. S6c) showed a reduction in peak

positions and intensities post-stability test, with the appearance of single broad peaks. Additionally, the Mo 3d_{5/2} and 3d_{3/2} peak positions shifted to higher binding energies, indicating a reducing crystallinity, and reducing Mo loading with conversion their hydroxides or oxides during HER in alkaline conditions [57]. The atomic percentage of Mo decreased from 1.48 to 0.88 (loss of 40.54 %), and the Mo/C atomic ratio fell from 2.00 to 1.16 % (loss of 42.0 %) after the stability test. Regarding the S 2p peaks (Fig. S6d), there was a significant reduction in intensity at 162.7 eV due to the formation of OH⁻ and H* on *h*-MoS₂ during the HER. Conversely, the intensity of the oxidized sulfur peak at 168.5 eV increased. Meanwhile, the C 1s and N 1s peaks (Fig. S6e–f) showed there is minimum changes compared to the pristine Pt–C core-shell@*h*-MoS₂/GNF.

3.4. In-situ Raman analysis

In-situ micro-Raman analysis is an analytical technique to investigate the hydrogen evolution reaction (HER) mechanism. This analysis provides the mechanisms of the changes of the formation of reaction intermediates, changes in the crystal structure, and the formation of defects during electrochemical performance [58,59]. We conducted *in-situ* Raman analysis using a confocal microscope Raman system (Horiba) with a laser wavelength of 532 nm and laser power about 0.9 mW along with a 50× objective lens and in situ Raman analysis set up shown in Fig. 4f. *In-situ* Raman analysis was carried out using a home-made electrochemical cell and kept at different constant potential for 200 s to achieve stable current before collection of the Raman spectrum (acquisition time of 10 s with 10 sweeps). The *in-situ* Raman spectra of Pt–C core-shell@*h*-MoS₂/GNF and *h*-MoS₂/GNF with different potential ranges of 0 to –0.2 V vs. RHE are shown in Fig. 4g and S7a. The Raman spectra of Pt–C core-shell@*h*-MoS₂/GNF (Fig. 4g) from the 0 to –0.2 V vs. RHE show MoS₂ characteristic peaks of 374 cm⁻¹, which belong to E_{2g} (Mo–S) due to in plane vibration within the S–Mo–S layer. The peak at 404 cm⁻¹ belongs to the vibration mode of A_{1g} due to in plane vibration within the S–Mo–S layer [58,60]. The intensities of E_{2g} and A_{1g} changed and there is no significant changes in peaks position during the different applied potential of 0 to –0.2 V vs RHE [58,60–62]. Furthermore, we investigated the HER mechanism of the MoS₂ using DFT analysis, confirming the formation of the absorption of the hydrogen on MoS₂ (see Section 3.5).

3.5. DFT calculations

3.5.1. Structure modeling

DFT-based first-principles calculations were performed to further explore structural stability of Pt₁₃–C₉₀ core-shell@*h*-MoS₂ and to find the active sites for HER on this hierarchical structure at the atomic scale, which is not accessible by experiments. The core consists of a Pt₁₃ atomic cluster, whereas the shell is made of C₉₀. Then, the Pt₁₃–C₉₀ core-shell structure deposited over the monolayer of *h*-MoS₂, mimicking the morphology of experimentally synthesized catalyst. In the experimental procedure, carbon fibers were used as a supporting material to deposit or grow the catalyst. The carbon fibers, which do not take part in HER, were not considered in the simulations. The structural model of the Pt–C core-shell particle is based on experimental information, and its size is about 1.3 nm. Although this size is a little smaller than the experimental value (ranging from 2 to 3 nm), the present DFT study focuses on the active sites at atomic scale and can capture the essential features of HER.

3.5.2. Structure optimization

As described in the structure modeling section, atomic positions of C₉₀ molecule (Fig. S8d) as a shell and Pt clusters with 10 and 13 atoms as two different cores were optimized separately. Using these optimized structures, Pt₁₃–C₉₀ core-shell (Fig. S8g) and Pt₁₀–C₉₀ core-shell were designed as core/shell structures. The calculations on core-shell structures revealed that Pt₁₃–C₉₀ had efficient atomic packing in terms of

void between core and shell when compared to the Pt₁₀–C₉₀ core-shell. Since ~5 % of carbon atoms in the shell were chemically replaced by nitrogen atoms based on the experiments, C_{90-x}N_x (x = 0 to 5) structures with and without Pt₁₃ core were considered and optimized to study the HER properties. Additionally, the stability of the simulated structures was tested with AIMD calculations using CONQUEST. It was observed that the structure of C_{90-x}N_x (x = 0 to 5) was stable during the AIMD simulations for 2 ps. The time profiles of temperature and potential energy during AIMD are shown in Fig. S9a and b. On the other hand, when the AIMD simulations were performed for Pt₁₃–C_{90-x}N_x core-shell with x = 0 to 5, Pt₁₃–C₉₀ and Pt₁₃–C₈₈N₂ core-shell structures were stable up to 2 ps (Fig. S9a and b) while the shells of Pt₁₃–C₈₇N₃, Pt₁₃–C₈₆N₄, and Pt₁₃–C₈₅N₅ structures were broken within 1 ps by opening the shell geometry (Ref Fig. S9c and d and atomic movies in the supporting materials). This suggests that increasing N concentration at the shell leads to structural instability.

Therefore Pt₁₃–C₈₈N₂ core-shells were selected to build a hierarchical structure by depositing a Pt₁₃–C₈₈N₂ core-shell particle on the *h*-MoS₂ sheet (Pt₁₃–C₈₈N₂@*h*-MoS₂). Monolayers of *h*-MoS₂ were chosen to model the *h*-MoS₂ sheet. The optimized lattice constant of *h*-MoS₂ is 3.237 Å, which is in good agreement with existing experimental value of $a = 3.25$ Å (Fig. S8a and b) [63]. A large supercell using this optimized *h*-MoS₂ monolayer was constructed to accommodate a Pt₁₃–C₈₈N₂ core-shell particle (Fig. S8i). AIMD simulation on Pt₁₃–C₈₈N₂@*h*-MoS₂ was performed to investigate the stability and the time profile of potential energy and temperature as shown in Fig. S9a and b. AIMD results show that the structure of Pt₁₃–C₈₈N₂@*h*-MoS₂ stays close to their optimized structure and the distance between the core-shell particle and the *h*-MoS₂ layer was about 4.2 Å. This optimized Pt₁₃–C₈₈N₂@*h*-MoS₂ was used to model the experimentally synthesized catalysts and to study their HER properties.

3.5.3. DFT calculation for HER studies

To understand the HER properties in Pt₁₃–C₈₈N₂@*h*-MoS₂ in detail, ΔG_{H^*} was calculated for each atomic site that is available in C₉₀, C₈₈N₂, C₈₅N₅, Pt₁₃–C₉₀, Pt₁₃–C₈₈N₂, and Pt₁₃–C₈₈N₂@*h*-MoS₂. An analysis of ΔG_{H^*} during the construction from C₉₀ to Pt₁₃–C₈₈N₂@*h*-MoS₂ (Fig. 5a–f) shows how HER non-active sites (mostly hydrogen desorption sites or energetically highly unstable hydrogen binding sites) at C₉₀ are converted into active sites for hydrogen adsorption/desorption at Pt₁₃–C₈₈N₂@*h*-MoS₂ by developing a hierarchical structure. The sites having ΔG_{H^*} near-zero or ranging from –0.2 to 0.2 eV can be considered as HER active [64]. The calculated ΔG_{H^*} values of C₉₀ highly depend on different carbon sites that are located at five or six membered carbon rings in the C₉₀ molecule. As shown in Fig. 5a, carbon sites with lower (<0.3 eV) and higher (>0.7 eV) ΔG_{H^*} values are directly connected with five and six-membered C rings of the C₉₀ molecule, respectively. Though the ΔG_{H^*} values between 0.3 and 0.7 eV belong to six-membered C rings, this variation from 0.3 to 0.7 eV is related to the distance of active sites from its nearest five-membered C ring. When ΔG_{H^*} was calculated for N sites in C₈₈N₂ and C₈₅N₅, hydrogen atoms were unstable with a ΔG_{H^*} higher than 1 eV (highly desorption nature). It is worth noting that H adsorption sites from five-membered rings in C₈₅N₅ become more stable as compared to that in C₉₀ when increasing N from C₈₈N₂ to C₈₅N₅ (Fig. 5b and c).

When Pt₁₃ core was introduced to C₉₀ shells, the optimized bond distances between Pt(core) and C(shell) are in the range from 2.15 to 2.30 Å. The calculated ΔG_{H^*} values of these structures show that more than 70 % of carbon sites fall between –0.2 and 0.2 eV of ΔG_{H^*} to become HER active sites. In the case of C₈₈N₂ shell with a Pt₁₃ core, 11 % more C sites became active than N-free Pt₁₃–C₉₀ core-shell structure and the ΔG_{H^*} corresponds to a few stronger H adsorption sites on C atoms due to doped N atoms. Except for two five-coordinated C sites bonded with N atoms shown in Fig. 5e, the free energies of other five-coordinated C sites bonded with N atoms were less than –2 eV. Most of the Pt sites at the core become unstable ($\Delta G_{H^*} > 2.0$ eV) for H

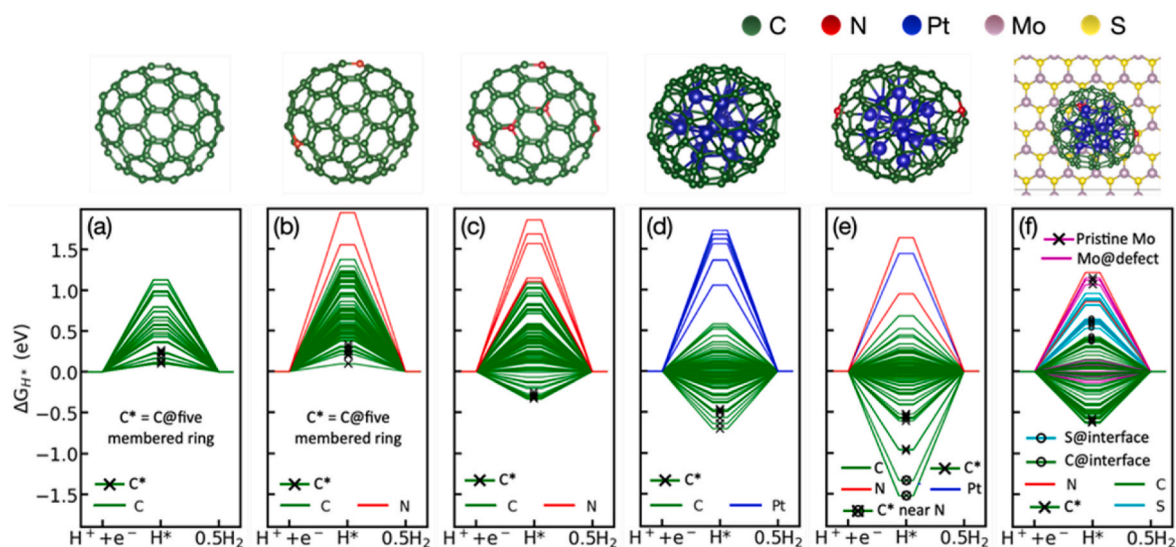


Fig. 5. Calculated reaction free energies of hydrogen adsorbed sites (ΔG_{H^*}) are plotted for the optimized structures (on top of each plot) starting from (a) C_{90} , (b) $C_{88}N_2$, (c) $C_{85}N_5$, (d) $Pt_{13}-C_{90}$, (e) $Pt_{13}-C_{88}N_2$, and (f) $Pt_{13}-C_{88}N_2@h-MoS_2$. (A colour version of this figure can be viewed online.)

adsorption except for a few sites that are shown in Fig. 5d and e. Finally, before calculating the free energy for $Pt_{13}-C_{88}N_2@h-MoS_2$, ΔG_{H^*} at Mo as well as S sites on pristine $h-MoS_2$ were calculated and found to be higher than 1 eV. At the same time, Mo atoms near S vacancy (Fig. 5f and Fig. S8j) participate in the HER activity as calculated free energies are in the range from 0.11 to -0.13 eV that are in good agreement with previous reports [20,21]. In addition to this, when $Pt_{13}-C_{88}N_2$ deposited on $h-MoS_2$, free energy at the sulfur atoms in the interface becomes ~ 0.5 eV (Ref. Fig. 5f), which is unlike pristine sulfur atoms that act as hydrogen unstable sites (or more than 0.75 eV of ΔG_{H^*}). Therefore, engineering of hierarchical structure, $Pt_{13}-C_{88}N_2@h-MoS_2$, produces comparatively more active sites and prevents agglomeration of core-shell structures that may decrease the surface area (and thus durability) of the catalyst.

3.6. AEM water electrolyzer performance of Pt-C core-shell@h-MoS₂/GNF

The excellent HER activity of prepared catalyst was further

confirmed in a full cell AEM water electrolyzer system as shown in Fig. 6a–d and Fig. S(10a–d), which show the full cell electrolyzer performance with the optimized Pt-C core-shell@h-MoS₂/GNF. Fig. 6a shows a schematic diagram of the AEM water electrolyzer cell. The AEM water electrolyzer was fabricated using an anode catalyst of NiCo₂O₄ (2 mg cm⁻²) and a cathode catalyst of Pt-C core-shell@h-MoS₂/GNF (Pt loading of 0.2 mg cm⁻²). The radiation grafted LPDE-VBC-TMA used as AEM and device fabrication details are provided in the experimental section. As expected, the cell performance (see Fig. 6b and c) increased with increasing temperature where the reaction kinetics and hydroxide transport were enhanced [65]. It is interesting to note that Pt-C core-shell@h-MoS₂/GNF||NiCo₂O₄ achieved a current density of 20 mA cm⁻² at 1.55 V in 1 M KOH at 60 °C, whereas the same current density was achieved at 1.64 V and 20 °C. Fig. 6b and c shows the effect of supporting electrolyte concentration on the cell performance. Diluting the supporting electrolyte by a factor of 10 improved the cell potential by just 30 mV compared to 1 M KOH, suggesting the possibility of operating over a wide range of pH. Area specific resistance (ASR) plays an

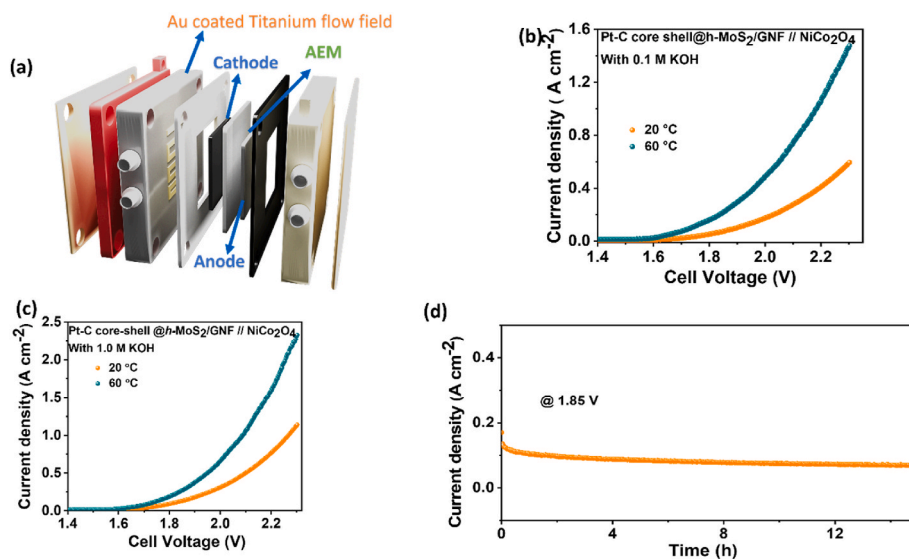


Fig. 6. AEM electrolyzers performance: (a) schematic diagram for AEM electrolyzer, AEM water electrolyzer performance with (b) 0.1 M and (c) 1.0 M electrolyte at 20 and 60 °C (Anode catalyst: NiCo₂O₄ (2 mg cm⁻²); Cathode: Pt-C core-shell@h-MoS₂/GNF (Pt loading 0.2 mg cm⁻²) and AEM LPDE-VBC-TMA), (d) stability test of AEM water electrolyzer @ 1.85 V for 15 h. (A colour version of this figure can be viewed online.)

important role in the improvement of the electrolyzer performance, and it is calculated from Fig. S10a–b. The bar chart shows the calculated ASR values with different temperature and concentrations of electrolytes. Further, Fig. S10a–c shows area specific resistance (ASR) values for the MEAs at 20 °C and 60 °C in 0.1 and 1 M KOH calculated from the high frequency intercept of the EIS spectra. It is noteworthy that a 38.80 % (0.090–0.055 $\Omega \text{ cm}^{-2}$) reduction in ASR was observed when the temperature increased from 20 °C to 60 °C in 0.1 M KOH, while a 52.22 % (0.090–0.043 $\Omega \text{ cm}^{-2}$) reduction ASR was observed when the concentration increased from 0.1 M to 1 M at 20 °C. The Pt–C core-shell@h-MoS₂/GNF||NiCo₂O₄ AEM water electrolyzer achieved a current density of 1000 mA cm⁻² at 2.08 V in 1 M KOH at 60 °C (See Table S5 comparison of AEM performance of Pt–C core-shell@h-MoS₂/GNF with recently reported catalysts), while a similar current density was achieved at 2.18 V 0.1 M KOH at 60 °C. The MEA was subjected to a constant potential at 1.85 V, and current density was measured for 15 h in 1 M KOH to examine the long-term use of the prepared catalysts, as shown in Fig. 6d. It is interesting to note that the cell initially showed a current density of 135 mA cm⁻², and a 22 % drop in current density was observed within the first hour of operation. On the other hand, only a 28 % drop was observed for the next 14 h. The initial drop in current density may be attributed to the change in electronic structure of the OER catalyst and the membrane activity.

The electrode architecture of Pt–C core-shell@h-MoS₂/GNF provide highly dispersed and stable Pt–C core-shell on the h-MoS₂/GNF. In addition, the inclusion of GNF furnished an efficient conductive pathway, thereby significantly enhancing the overall performance of the AEM water electrolyzer. Finally, we used precious anode electrode catalyst (IrO₂) and fabricated an AEM water electrolyzer Pt–C core-shell@h-MoS₂/GNF|| IrO₂. The LSV polarization curves are shown in Fig. S10d.

4. Conclusion

In conclusion, addressing the critical need for low cost, active and durable electrocatalyst for AEM water electrolyzers is an essential task to achieve net zero emission and decarbonization goal in coming decades. In this study, we successfully synthesized hierarchical MoS₂ coated graphitic nanofiber (h-MoS₂/GNF) supported Pt–C core-shell structure with Pt-loading of 11.3 %, compared to the 20 % Pt-loading in commercial Pt–C. Experimental findings indicated that the synthesized Pt–C core-shell@h-MoS₂/GNF exhibited 26.8 % lower HER overpotential, achieving 30 mV at 10 mA cm⁻² as compared to commercial 20 % Pt–C (41 mV at 10 mA cm⁻²). This improvement is attributed to the highly dispersed and stable Pt nanoparticles, potentially due to the supporting framework, the carbon shell, or a combination of both. Furthermore, DFT simulations provided an atomic level understanding of Pt–C core-shell and interface of core-shell@h-MoS₂ structures, as well as HER mechanism. To practical aspect, cathode catalyst of Pt–C core-shell@h-MoS₂/GNF with AEM water electrolyzer, achieved cell current density of 1 A cm⁻² at 2.08 V 1 M KOH at 60 °C and comparable stability up to 14 h @ 1.85 V. This present work provides a new pathway to designing innovative core-shell electrocatalysts with reduced Pt-loading, thereby decreasing the cost of the anode catalyst for AEM water electrolyzers and promoting the generation of green hydrogen.

Data availability

The data supporting the findings of this study are available within the article and its Supplementary Information.

CRediT authorship contribution statement

Shanmugam Ramakrishnan: Conceptualization, Data curation, Formal analysis, Funding acquisition, Investigation, Methodology, Project administration, Resources, Supervision, Writing – original draft,

Writing – review & editing. **Subramanian Vijayapradeep:** Data curation, Software, Validation, Visualization, Writing – review & editing. **Selva Chandrasekaran Selvaraj:** Data curation, Formal analysis, Investigation, Software, Writing – original draft, Writing – review & editing. **Jian Huang:** Data curation, Visualization, Writing – review & editing. **S.C. Karthikeyan:** Validation, Visualization, Writing – review & editing. **Rambabu Gutru:** Data curation, Visualization, Writing – review & editing. **Natarajan Logeshwaran:** Visualization, Writing – review & editing. **Tsuyoshi Miyazaki:** Software, Supervision, Writing – review & editing. **Mohamed Mamlouk:** Data curation, Supervision, Funding acquisition, Writing – review & editing. **Dong Jin Yoo:** Funding acquisition, Project administration, Resources, Supervision, Validation, Visualization, Writing – review & editing.

Declaration of competing interest

The authors declare that they have no known competing financial interests or personal relationships that could have appeared to influence the work reported in this paper.

Acknowledgments

This work was supported by BK21 FOUR Program by Jeonbuk National University, South Korea, Research Grant. This research was supported by Basic Science Research through the National Research Foundation of Korea (NRF) funded by the Ministry of Education (NRF-2022R1A2C1012300). This research was supported by “Regional Innovation Strategy (RIS)” through the National Research Foundation of Korea (NRF) funded by the Ministry of Education (MOE) (2023RIS-008). This work was supported by grants from the Ocean Renewable Energy Fuel (Ocean-REFuel) project with grant number EP/W005204/1 funded by the UK Research and Innovation (UKRI), United Kingdom.

Appendix A. Supplementary data

Supplementary data to this article can be found online at <https://doi.org/10.1016/j.carbon.2024.118816>.

References

- [1] S. Ramakrishnan, J. Balamurugan, M. Vinothkannan, A.R. Kim, S. Sengodan, D. J. Yoo, Nitrogen-doped graphene encapsulated FeCoMoS nanoparticles as advanced trifunctional catalyst for water splitting devices and zinc–air batteries, *Appl. Catal., B* 279 (2020) 119381.
- [2] T.F. Jaramillo, K.P. Jørgensen, J. Bonde, J.H. Nielsen, S. Horch, I. Chorkendorff, Identification of active edge sites for electrochemical H₂ evolution from MoS₂ nanocatalysts, *Science* 317 (5834) (2007) 100–102.
- [3] J. Greeley, T.F. Jaramillo, J. Bonde, I. Chorkendorff, J.K. Nørskov, Computational high-throughput screening of electrocatalytic materials for hydrogen evolution, *Nat. Mater.* 5 (11) (2006) 909–913.
- [4] H. Xie, Z. Zhao, T. Liu, Y. Wu, C. Lan, W. Jiang, L. Zhu, Y. Wang, D. Yang, Z. Shao, A membrane-based seawater electrolyser for hydrogen generation, *Nature* 612 (7941) (2022) 673–678.
- [5] T.J. Bandoz, Revealing the impact of small pores on oxygen reduction on carbon electrocatalysts: a journey through recent findings, *Carbon* 188 (2022) 289–304.
- [6] K.Y. Yap, H.H. Chin, J.J. Klemes, Solar energy-powered battery electric vehicle charging stations: current development and future prospect review, *Renewable Sustainable Energy Rev.* 169 (2022) 112862.
- [7] D.V. Jawale, F. Fossard, F. Miserque, V. Geertsen, A.-L. Teillout, P. de Oliveira, I. M. Mbomekallé, E. Gravel, E. Doris, Carbon nanotube-polyoxometalate nanohybrids as efficient electro-catalysts for the hydrogen evolution reaction, *Carbon* 188 (2022) 523–532.
- [8] A.J. Shih, M.C.O. Monteiro, F. Dattila, D. Pavesi, M. Phillips, A.H.M. da Silva, R. E. Vos, K. Ojha, S. Park, O. van der Heijden, G. Marcandalli, A. Goyal, M. Villalba, X. Chen, G.T.K.K. Gunasooriya, I. McCrum, R. Mom, N. López, M.T.M. Koper, Water electrolysis, *Nat. Rev. Methods Primers* 2 (1) (2022) 84.
- [9] R. Thimmappa, D. Walsh, K. Scott, M. Mamlouk, Diethylmethylammonium trifluoromethanesulfonate protic ionic liquid electrolytes for water electrolysis, *J. Power Sources* 449 (2020) 227602.
- [10] R. Thimmappa, K. Scott, M. Mamlouk, A diethyl methyl ammonium triflate based protic ionic liquid polymer membrane for intermediate temperature water electrolysis, *Int. J. Hydrogen Energy* 45 (53) (2020) 28303–28312.
- [11] S.C. Karthikeyan, R. Santhosh Kumar, S. Ramakrishnan, S. Prabhakaran, A.R. Kim, D.H. Kim, D.J. Yoo, Efficient alkaline water/seawater electrolysis by development

- of ultra-low IrO₂ nanoparticles decorated on hierarchical MnO₂/rGO nanostructure, *ACS Sustainable Chem. Eng.* 10 (46) (2022) 15068–15081.
- [12] N. Lageshwaran, S. Ramakrishnan, S.S. Chandrasekaran, M. Vinothkannan, A. R. Kim, S. Sengodan, D.B. Velusamy, P. Varadhan, J.-H. He, D.J. Yoo, An efficient and durable trifunctional electrocatalyst for zinc–air batteries driven overall water splitting, *Appl. Catal., B* 297 (2021) 120405.
- [13] X. Han, X. Wu, Y. Deng, J. Liu, J. Lu, C. Zhong, W. Hu, Ultrafine Pt nanoparticle-decorated Pyrite-Type CoS₂ nanosheet arrays coated on carbon cloth as a bifunctional electrode for overall water splitting, *Adv. Energy Mater.* 8 (24) (2018) 1800935.
- [14] J. Zhu, Y. Tu, L. Cai, H. Ma, Y. Chai, L. Zhang, W. Zhang, Defect-assisted anchoring of Pt single atoms on MoS₂ nanosheets produces high-performance catalyst for industrial hydrogen evolution reaction, *Small* 18 (4) (2022) 2104824.
- [15] C.-H. An, W. Kang, Q.-B. Deng, N. Hu, Pt and Te codoped ultrathin MoS₂ nanosheets for enhanced hydrogen evolution reaction with wide pH range, *Rare Met.* 41 (2) (2022) 378–384.
- [16] J. Rong, G. Zhu, W. Ryan Osterloh, Y. Fang, Z. Ou, F. Qiu, K.M. Kadish, In situ construction MoS₂-Pt nanosheets on 3D MOF-derived S, N-doped carbon substrate for highly efficient alkaline hydrogen evolution reaction, *Chem. Eng. J.* 412 (2021) 127556.
- [17] A. Ashok, A. Kumar, J. Ponraj, S.A. Mansour, Synthesis and growth mechanism of bamboo like N-doped CNT/Graphene nanostructure incorporated with hybrid metal nanoparticles for overall water splitting, *Carbon* 170 (2020) 452–463.
- [18] D. Wu, Y. Wang, F. Wang, H. Wang, Y. An, Z. Gao, F. Xu, K. Jiang, Oxygen-incorporated few-layer MoS₂ vertically aligned on three-dimensional graphene matrix for enhanced catalytic performances in quantum dot sensitized solar cells, *Carbon* 123 (2017) 756–766.
- [19] Z. Xiang, Z. Zhang, X. Xu, Q. Zhang, C. Yuan, MoS₂ nanosheets array on carbon cloth as a 3D electrode for highly efficient electrochemical hydrogen evolution, *Carbon* 98 (2016) 84–89.
- [20] G. Li, D. Zhang, Q. Qiao, Y. Yu, D. Peterson, A. Zafar, R. Kumar, S. Curtarolo, F. Hunte, S. Shannon, Y. Zhu, W. Yang, L. Cao, All the catalytic active sites of MoS₂ for hydrogen evolution, *J. Am. Chem. Soc.* 138 (51) (2016) 16632–16638.
- [21] H. Li, C. Tsai, A.L. Koh, L. Cai, A.W. Contryman, A.H. Fragapane, J. Zhao, H.S. Han, H.C. Manoharan, F. Abild-Pedersen, J.K. Nørskov, X. Zheng, Activating and optimizing MoS₂ basal planes for hydrogen evolution through the formation of strained sulphur vacancies, *Nat. Mater.* 15 (1) (2016) 48–53.
- [22] H. Nolan, C. Schröder, M. Brunet-Cabrè, F. Pota, N. McEvoy, K. McKelvey, T. S. Perova, P.E. Colavita, MoS₂/carbon heterostructured catalysts for the hydrogen evolution reaction: N-doping modulation of substrate effects in acid and alkaline electrolytes, *Carbon* 202 (2023) 70–80.
- [23] A. Rajapriya, S. Keerthana, C. Viswanathan, N. Ponpandian, Direct growth of MoS₂ hierarchical nanoflowers on electrospun carbon nanofibers as an electrode material for high-performance supercapacitors, *J. Alloys Compd.* 859 (2021) 157771.
- [24] M. Karuppannan, Y. Kim, S. Gok, E. Lee, J.Y. Hwang, J.-H. Jang, Y.-H. Cho, T. Lim, Y.-E. Sung, O.-J. Kwon, A highly durable carbon-nanofiber-supported Pt–C core–shell cathode catalyst for ultra-low Pt loading proton exchange membrane fuel cells: facile carbon encapsulation, *Energy Environ. Sci.* 12 (9) (2019) 2820–2829.
- [25] S. Ramakrishnan, D.B. Velusamy, S. Sengodan, G. Nagaraju, D.H. Kim, A.R. Kim, D. J. Yoo, Rational design of multifunctional electrocatalyst: an approach towards efficient overall water splitting and rechargeable flexible solid-state zinc–air battery, *Appl. Catal., B* 300 (2022) 120752.
- [26] Z. Wu, Y. Lv, Y. Xia, P.A. Webley, D. Zhao, Ordered mesoporous platinum@graphitic carbon embedded nanophase as a highly active, stable, and methanol-tolerant oxygen reduction electrocatalyst, *J. Am. Chem. Soc.* 134 (4) (2012) 2236–2245.
- [27] Y. Zhang, H. Huang, Y. Han, Y. Qin, N. Nie, W. Cai, X. Zhang, Z. Li, J. Lai, L. Wang, Constructing stable charge redistribution through strong metal–support interaction for overall water splitting in acidic solution, *J. Mater. Chem. A* 10 (25) (2022) 13241–13246.
- [28] C. Zhai, M. Zhu, D. Bin, F. Ren, C. Wang, P. Yang, Y. Du, Two dimensional MoS₂/graphene composites as promising supports for Pt electrocatalysts towards methanol oxidation, *J. Power Sources* 275 (2015) 483–488.
- [29] B. Tang, Y. Lin, Z. Xing, Y. Duan, S. Pan, Y. Dai, J. Yu, J. Zou, Porous coral reefs-like MoS₂/nitrogen-doped bio-carbon as an excellent Pt support/co-catalyst with promising catalytic activity and CO-tolerance for methanol oxidation reaction, *Electrochim. Acta* 246 (2017) 517–527.
- [30] G. Gupta, K. Scott, M. Mamlouk, Performance of polyethylene based radiation grafted anion exchange membrane with polystyrene-*b*-poly (ethylene/butylene)-*b*-polystyrene based ionomer using NiCo₂O₄ catalyst for water electrolysis, *J. Power Sources* 375 (2018) 387–396.
- [31] M. Mamlouk, J.A. Horsfall, C. Williams, K. Scott, Radiation grafted membranes for superior anion exchange polymer membrane fuel cells performance, *Int. J. Hydrogen Energy* 37 (16) (2012) 11912–11920.
- [32] D.R. Bowler, T. Miyazaki, Calculations for millions of atoms with density functional theory: linear scaling shows its potential, *J. Phys. Condens. Matter* 22 (7) (2010) 074207.
- [33] T. Miyazaki, D.R. Bowler, R. Choudhury, M.J. Gillan, Atomic force algorithms in density functional theory electronic-structure techniques based on local orbitals, *J. Chem. Phys.* 121 (13) (2004) 6186–6194.
- [34] D.R. Bowler, R. Choudhury, M.J. Gillan, T. Miyazaki, Recent progress with large-scale ab initio calculations: the CONQUEST code, *Phys. Stat. Sol.* 243 (5) (2006) 989–1000.
- [35] J.P. Perdew, K. Burke, M. Ernzerhof, Generalized gradient approximation made simple, *Phys. Rev. Lett.* 77 (18) (1996) 3865–3868.
- [36] S. Grimme, Semiempirical GGA-type density functional constructed with a long-range dispersion correction, *J. Comput. Chem.* 27 (15) (2006) 1787–1799.
- [37] D.R. Bowler, J.S. Baker, J.T.L. Poulton, S.Y. Mujahed, J. Lin, S. Yadav, Z. Raza, T. Miyazaki, Highly accurate local basis sets for large-scale DFT calculations in conquest, *Jpn. J. Appl. Phys.* 58 (10) (2019) 100503.
- [38] J.K. Nørskov, T. Bligaard, A. Logadottir, J.R. Kitchin, J.G. Chen, S. Pandalov, U. Stimming, Trends in the exchange current for hydrogen evolution, *J. Electrochem. Soc.* 152 (3) (2005) J23.
- [39] J.N. Tiwari, A.M. Harzandi, M. Ha, S. Sultan, C.W. Myung, H.J. Park, D.Y. Kim, P. Thangavel, A.N. Singh, P. Sharma, S.S. Chandrasekaran, F. Salehnia, J.-W. Jang, H.S. Shin, Z. Lee, K.S. Kim, High-performance hydrogen evolution by Ru single atoms and nitrided-ru nanoparticles implanted on N-doped graphitic sheet, *Adv. Energy Mater.* 9 (26) (2019) 1900931.
- [40] R. Kronberg, M. Hakala, N. Holmberg, K. Laasonen, Hydrogen adsorption on MoS₂-surfaces: a DFT study on preferential sites and the effect of sulfur and hydrogen coverage, *Phys. Chem. Chem. Phys.* 19 (24) (2017) 16231–16241.
- [41] M. Arita, D.R. Bowler, T. Miyazaki, Stable and efficient linear scaling first-principles molecular dynamics for 10000+ atoms, *J. Chem. Theor. Comput.* 10 (12) (2014) 5419–5425.
- [42] T. Hirakawa, T. Suzuki, D.R. Bowler, T. Miyazaki, Canonical-ensemble extended Lagrangian Born–Oppenheimer molecular dynamics for the linear scaling density functional theory, *J. Phys. Condens. Matter* 29 (40) (2017) 405901.
- [43] Y. Kim, H.E. Bae, D. Lee, J. Kim, E. Lee, S. Oh, J.-H. Jang, Y.-H. Cho, M. Karuppannan, Y.-E. Sung, T. Lim, O.-J. Kwon, High-performance long-term driving proton exchange membrane fuel cell implemented with chemically ordered Pt-based alloy catalyst at ultra-low Pt loading, *J. Power Sources* 533 (2022) 231378.
- [44] S. Ramakrishnan, M. Karuppannan, M. Vinothkannan, K. Ramachandran, O. J. Kwon, D.J. Yoo, Ultrafine Pt nanoparticles stabilized by MoS₂/N-doped reduced graphene oxide as a durable electrocatalyst for alcohol oxidation and oxygen reduction reactions, *ACS Appl. Mater. Interfaces* 11 (13) (2019) 12504–12515.
- [45] A.C. Ferrari, J. Robertson, Interpretation of Raman spectra of disordered and amorphous carbon, *Phys. Rev. B* 61 (20) (2000) 14095–14107.
- [46] H.-J. Kim, D. Kim, S. Jung, M.-H. Bae, Y.J. Yun, S.N. Yi, J.-S. Yu, J.-H. Kim, D. H. Ha, Changes in the Raman spectra of monolayer MoS₂ upon thermal annealing, *J. Raman Spectrosc.* 49 (12) (2018) 1938–1944.
- [47] T. Nisar, T. Balster, V. Wagner, Mechanical transfer of electrochemically grown molybdenum sulfide layers to silicon wafer, *J. Appl. Electrochem.* 51 (9) (2021) 1279–1286.
- [48] Z. Xie, S. Yu, X. Ma, K. Li, L. Ding, W. Wang, D.A. Cullen, H.M. Meyer, H. Yu, J. Tong, Z. Wu, F.-Y. Zhang, MoS₂ nanosheet integrated electrodes with engineered 1T-2H phases and defects for efficient hydrogen production in practical PEM electrolysis, *Appl. Catal., B* 313 (2022) 121458.
- [49] M. Alamri, R. Sakidja, R. Goul, S. Ghopy, J.Z. Wu, Plasmonic Au nanoparticles on 2D MoS₂/Graphene van der Waals heterostructures for high-sensitivity Surface-Enhanced Raman Spectroscopy, *ACS Appl. Nano Mater.* 2 (3) (2019) 1412–1420.
- [50] D. Long, W. Li, L. Ling, J. Miyawaki, I. Mochida, S.-H. Yoon, Preparation of nitrogen-doped graphene sheets by a combined chemical and hydrothermal reduction of graphene oxide, *Langmuir* 26 (20) (2010) 16096–16102.
- [51] S.H. Patil, B. Anothumakkool, S.D. Sathaye, K.R. Patil, Architecturally designed Pt–MoS₂ and Pt–graphene composites for electrocatalytic methanol oxidation, *Phys. Chem. Chem. Phys.* 17 (39) (2015) 26101–26110.
- [52] A. Shan, X. Teng, Y. Zhang, P. Zhang, Y. Xu, C. Liu, H. Li, H. Ye, R. Wang, Interfacial electronic structure modulation of Pt–MoS₂ heterostructure for enhancing electrocatalytic hydrogen evolution reaction, *Nano Energy* 94 (2022) 106913.
- [53] T. Shinagawa, A.T. Garcia-Esparza, K. Takanabe, Insight on Tafel slopes from a microkinetic analysis of aqueous electrocatalysis for energy conversion, *Sci. Rep.* 5 (1) (2015) 13801.
- [54] P. Connor, J. Schuch, B. Kaiser, W. Jaegermann, The determination of electrochemical active surface area and specific capacity revisited for the system MnO_x as an oxygen evolution catalyst, *Z. Phys. Chem.* 234 (5) (2020) 979–994.
- [55] M. Wang, L. Zhang, Y. He, H. Zhu, Recent advances in transition-metal-sulfide-based bifunctional electrocatalysts for overall water splitting, *J. Mater. Chem. A* 9 (9) (2021) 5320–5363.
- [56] M. Liu, J.-A. Wang, W. Klysubun, G.-G. Wang, S. Sattayaporn, F. Li, Y.-W. Cai, F. Zhang, J. Yu, Y. Yang, Interfacial electronic structure engineering on molybdenum sulfide for robust dual-pH hydrogen evolution, *Nat. Commun.* 12 (1) (2021) 5260.
- [57] M. Liu, J.-A. Wang, W. Klysubun, G.-G. Wang, S. Sattayaporn, F. Li, Y.-W. Cai, F. Zhang, J. Yu, Y. Yang, Interfacial electronic structure engineering on molybdenum sulfide for robust dual-pH hydrogen evolution, *Nat. Commun.* 12 (1) (2021) 5260.
- [58] Y. Li, R. Nakamura, Structural change of molybdenum sulfide facilitates the electrocatalytic hydrogen evolution reaction at neutral pH as revealed by in situ Raman spectroscopy, *Chin. J. Catal.* 39 (3) (2018) 401–406.
- [59] L. Ma, M. Liu, D. Jing, L. Guo, Photocatalytic hydrogen production over CdS: effects of reaction atmosphere studied by in situ Raman spectroscopy, *J. Mater. Chem. A* 3 (10) (2015) 5701–5707.
- [60] Y. Deng, L.R.L. Ting, P.H.L. Neo, Y.-J. Zhang, A.A. Peterson, B.S. Yeo, Operando Raman spectroscopy of amorphous molybdenum sulfide (MoS_x) during the electrochemical hydrogen evolution reaction: identification of sulfur atoms as catalytically active sites for H⁺ reduction, *ACS Catal.* 6 (11) (2016) 7790–7798.
- [61] S. Guo, Y. Li, S. Tang, Y. Zhang, X. Li, A.J. Sobrido, M.-M. Titirici, B. Wei, Monitoring hydrogen evolution reaction intermediates of transition metal

- dichalcogenides via operando Raman spectroscopy, *Adv. Funct. Mater.* 30 (35) (2020) 2003035.
- [62] Z. Li, C. Peng, H. Yin, Y. Ruan, Y. Sun, H. Chen, S. Yang, G. Cheng, Effects of structural changes on the enhanced hydrogen evolution reaction for Pd NPs @ 2H-MoS₂ studied by in-Situ Raman spectroscopy, *Chem. Phys. Lett.* 764 (2021) 138267.
- [63] G. Anemone, A. Al Taleb, A. Castellanos-Gomez, D. Fariñas, Experimental determination of thermal expansion of natural MoS₂, *2D Mater.* 5 (3) (2018) 035015.
- [64] J.N. Tiwari, S. Sultan, C.W. Myung, T. Yoon, N. Li, M. Ha, A.M. Harzandi, H. J. Park, D.Y. Kim, S.S. Chandrasekaran, W.G. Lee, V. Vij, H. Kang, T.J. Shin, H. S. Shin, G. Lee, Z. Lee, K.S. Kim, Multicomponent electrocatalyst with ultralow Pt loading and high hydrogen evolution activity, *Nat. Energy* 3 (9) (2018) 773–782.
- [65] G. Gupta, K. Selvakumar, N. Lakshminarasimhan, S.M. Senthil Kumar, M. Mamlouk, The effects of morphology, microstructure and mixed-valent states of MnO₂ on the oxygen evolution reaction activity in alkaline anion exchange membrane water electrolysis, *J. Power Sources* 461 (2020) 228131.